Hindawi
Advances in Materials Science and Engineering
Volume 2019, Article ID 1690512, 13 pages
https://doi.org/10.1155/2019/1690512

Research Article

Flexural Behavior of Hybrid Composite Beam (HCB) Bridges

Mohamed A. Aboelseoud[1] and John J. Myers[2]

[1]*Missouri University of Science and Technology, Rolla, MO 65409, USA*
[2]*Associate Dean for the College of Engineering and Computing and Professor of Civil, Architectural and Environmental Engineering, Missouri University of Science and Technology, Rolla, MO 65409, USA*

Correspondence should be addressed to John J. Myers; jmyers@mst.edu

Received 15 June 2018; Accepted 10 February 2019; Published 3 March 2019

Academic Editor: Carlos R. Rambo

A new hybrid composite beam (HCB) has recently been used in the construction of three bridges in Missouri, USA. HCB consists of self-consolidating concrete (SCC) that is poured into classical arch shape and tied at the ends by steel tendons. Both the concrete and the steel are tucked inside a durable fiberglass shell, and the voids are filled with polyiso foam. This paper aims to examine the flexural behavior of an in-service HCB, evaluate the current methodology and assumptions, and propose modifications to that methodology. To achieve these goals, the strains induced in HCB elements due to different loading stages were experimentally measured. Numerical predictions of the strains were performed via the existing methodology, the modified procedure, and a finite element model (FEM) that was constructed using ANSYS V14. The linear FEM predicted the strains with acceptable accuracy. The model clarified that the foam achieves partial composite action between the HCB elements, resulting in a strain incompatibility between them. The current methodology was found to be unable to predict the maximum compressive strain in the concrete arch. The modified procedure is based on the strain compatibility assumption. However, it models the HCBs as curved beam rather than a straight one, using a simplified spring model to represent the beam supports. These modifications achieved significant enhancements in estimating the strains under service loads.

1. Introduction

Fiber reinforced polymer (FRP) composites are extensively used as construction material in applications ranging from externally bonded laminates for strengthening and upgrading of existing infrastructures, wraps for seismic retrofit of columns, internal reinforcement bars, grids, and prestressing tendons to all-composite structural systems. Their extraordinary properties such as high strength-to-weight ratio, corrosion resistance, dimensional stability, excellent durability, transparency to electromagnetic radiation, and low to moderate tooling costs make them ideal alternatives for resolving a number of problems facing highway bridges, particularly corrosion and deterioration. However, fully composite FRP structural members fail to be cost competitive compared to traditional concrete and steel members used in civil engineering applications. This increased initial cost can be traced directly to the raw material costs and low stiffness of FRP composites. The most effective use of the FRP, as primary load carrying members, is found to be in the form of hybrid systems comprised of FRP and traditional construction materials [1].

A new type of HCB has recently been used to construct three bridges (B0439, B0410, and B0478) in MO, USA. The underlying concept of the HCB was conceived by Hillman in 1996 [2]. The HCB consists of a self-consolidating concrete (SCC) arch that is tied at the ends using high-strength galvanized steel strands. The concrete and steel, which present the compression and tension reinforcement, respectively, are encased inside a durable fiberglass composite shell. Due to this unique configuration, the glass fiber reinforced polymer (GFRP) box protects the steel and concrete from the environmental effects and serves as the formwork for the concrete arch, while the strength and stiffness are provided by an efficient use of the steel in purely axial tension and the concrete in purely axial compression. In addition to the optimization of load carrying behavior offered by this configuration, it results in a lightweight

member that can be transported easily and erected rapidly making this technology well suited to Accelerated Bridge Construction (ABC).

A limited number of research studies have been implemented on the HCB [3–9]. The results gathered from these studies demonstrate that the structural behavior of the HCB is not completely understood. Recent studies performed by [3, 4] revealed that the current design methodology is unable to predict the normal strains correctly at some locations indicating that the design methodology may need refinement. Thus, the primary objectives of this work to analyze the flexural behavior of in-service HCB under service loads, evaluate the current design methodology and assumptions, and introduce refinements to the current procedure. As a part of this investigation, HCB elements in bridge 0410 were instrumented with various sensors. The induced strains when the concrete arch poured, and under several load cases, were measured experimentally and predicted analytically. The numerical predictions were then compared to the field data.

2. Bridge 0410

Bridge 0410 was the second HCB Bridge to be constructed in Missouri. B0410 HCBs are the longest span HCBs yet constructed. B0410 spans 31.7 m (1248–in.), and its out-to-out dimension of the deck is 9.35 m (368–in.). B0410 consists of a simply supported single-span HCBs. Due to their long spans, the beams were fabricated as multicelled, double-web, beams to significantly reduce the time of fabrication and erection.

Each multicelled HCB has an overall depth of 152.4 cm (60–in.) and a varying width ranging from 167.6 cm (66–in) at the bottom to 182.9 cm (72–in.) at the top. Each single HCB consists of an SCC arch with 25.4 cm (10–in.) depth and 26.7 cm (10.5–in.) width. The concrete arch is reinforced with 2–12.7 mm (2–1/2–in.) diameter, 1.72 GPa (270 ksi) seven-wire galvanized steel strands. It is tied via 44-12.7 mm (44–1/2–in.) diameter, 1.72 GPa (270 ksi) steel strands arranged in two layers. The entire system is encapsulated in a GFRP shell with 152.4 cm (60–in.) depth and 34.9 cm (13.75–in.) width. The concrete arch is connected to the upper GFRP flange with a SCC web of varying width, and the voids were filled with polyisocyarunate (polyiso) foam. A typical cross section of B0410 is depicted in Figure 1.

3. Load Testing and Instrumentation of Bridge 0410

Structural elements of HCB2 were instrumented using different strain gauges to allow for the evaluation of the design procedure. These sensors allow also for the monitoring of the short-term and long-term behaviors of the HCB. Four electrical resistance strain gauges were adhered to tension strands. A concrete arch and its web were instrumented using nine vibrating wire strain gauges (VWSGs)/thermistors (seven gauges to measure normal strains and two gauges to measure shear strains). Twelve electrical resistance strain gauges were adhesively bonded to the FRP shell (seven sensors to measure normal strains and five to measure shear strains). Twelve thermocouples were placed at various locations. All but the FRP shell sensors were placed during the shell fabrication at Harbor Technologies, Maine, USA. The FRP strain gauges were placed on the shell by researchers from Missouri University of Science and Technology (Missouri S&T) prior to the concrete pour at the precast plant in Virginia, USA. Following fabrication, data collection indicated that two strand strain gauges and two VWSGs within the concrete arch were not functioning properly. While uncertain, these sensors could have been damaged due to the exposure to very high temperature during the resin infusion process or during the transportation and erection processes. Figure 2 displays the locations of the sensors within the member. Only the functional normal strain sensors are displayed in this figure. The VWSGs placed in the concrete are denoted by C and the FRP gauges are denoted by F, while the strand gauges are denoted by S.

Due to the construction sequence of the HCB bridges, the beam is subjected to three stages of dead and live loading. In the first stage, both the GFRP shell and the strands are subjected to stresses from casting the concrete arch and web. In the second stage, the noncomposite HCB is subjected to a load result from the deck and barriers pour. In the third stage, the composite HCB is subjected to a live load from in-service traffic.

Strain readings were taken an hour before the concrete arch was poured and continued for 25-hours. The initial strain data was subtracted from the strain readings recorded at the end of the arch pour. This provided the strains induced in the shell and strands due to stage 1 loads. Unfortunately, no data was collected while the deck was being poured (stage 2).

A load test was conducted with two fully loaded, ten-wheel, three-axle trucks to simulate stage 3 loading. These trucks performed three stops, simulating three different load cases. The stops were selected to produce maximum bending moments and shear forces in HCB2. Figure 3 illustrates the stops performed. The front axle load (P1) of the first truck (T-1995) was 7.48 metric tons (16.48 kip), the middle axle load (P2) was 7.07 metric tons (15.58 kip), and the rear axle load (P3) was 11.07 metric tons (24.4 kip). The P1 of the second truck (T-2406) equaled 7.45 metric tons (16.42 kip), the P2 equaled 9.31 metric tons (20.52 kip), and the P3 equaled 9.09 metric tons (20.04 kip).

The traffic was stopped, and initial strain measurements were recorded before performing the three stops. As in the first stage, these strains served as baseline and were subtracted from the strains induced by the three stops. Hence, the strains induced in the HCB2 elements due to pure live loading were obtained.

4. Material Properties

A MATLAB code was constructed to calculate the normal strains in HCB2. The code accounted for the material nonlinearity; however, the mathematical calculations showed that all the materials behaved within their elastic ranges under the applied loads. Consequently, only the

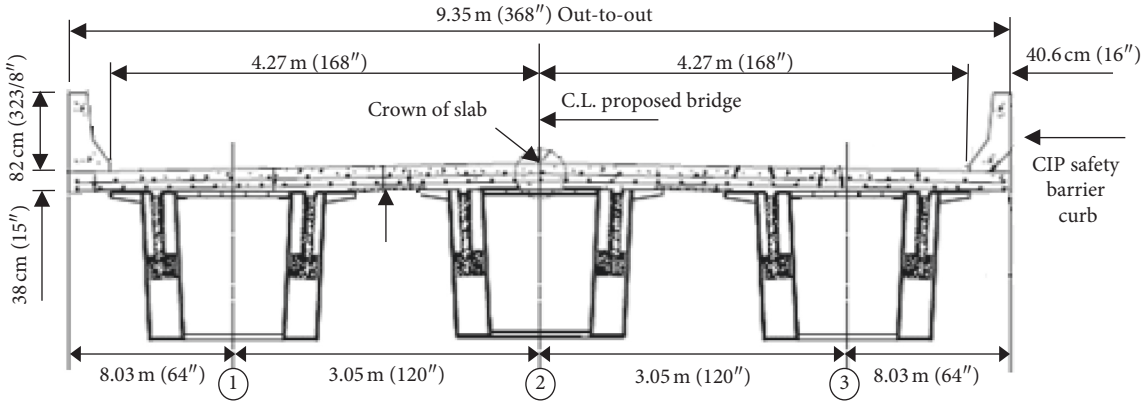

Figure 1: Typical cross section of bridge 0410.

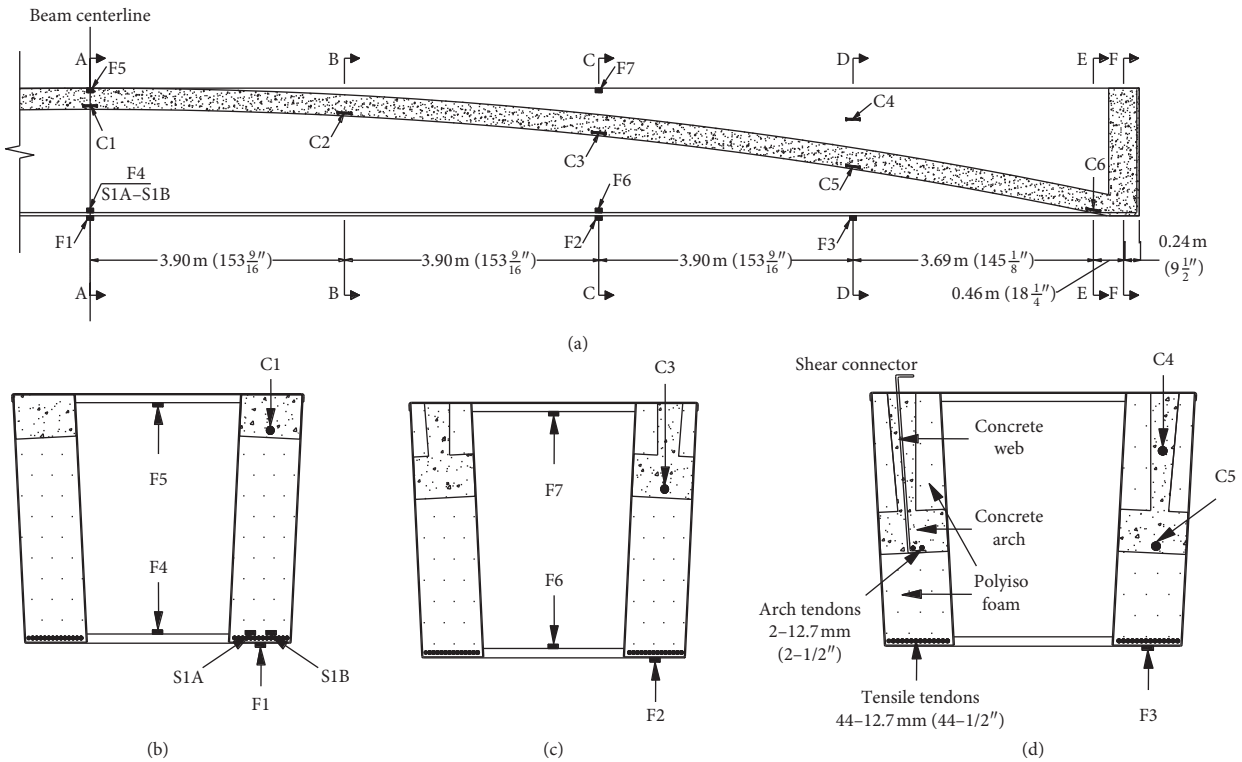

Figure 2: HCB2 instrumentation. (a) HCB2 elevation. (b) Section A-A. (c) Section C-C. (d) Section D-D.

linear properties of the constituent materials are presented in the following sections.

4.1. Concrete. In B0410, SCC was used to form the compression reinforcement of the HCBs. The field tests showed that the average compressive strength of the concrete arches of the HCBs was about 75.8 MPa (11 ksi). Since quality control specimens were not available to obtain specific concrete properties, based on a previous study [10], the traditional equations used with the normally vibrated concrete were used in the current study to calculate the SCC properties.

The current methodology assumes that the concrete below the neutral axis (NA) has cracked. In the current study, the concrete subjected to tensile stress was assumed to contribute to the strength and stiffness of the HCB up to the modulus of rupture of the concrete. This aimed to allow the comparison between the tensile strains captured by some sensors in the arch and the estimated strains. The elastic modulus, E_c, and the modulus of rupture, f_r, were calculated using the ACI 318-11 [11] equations in American Standard English (ASE) units from the standard:

$$E_c = 57000\sqrt{f'_c}\,(\text{ASE}), \tag{1}$$

$$f_r = 7.5\sqrt{f'_c}\,(\text{ASE}), \tag{2}$$

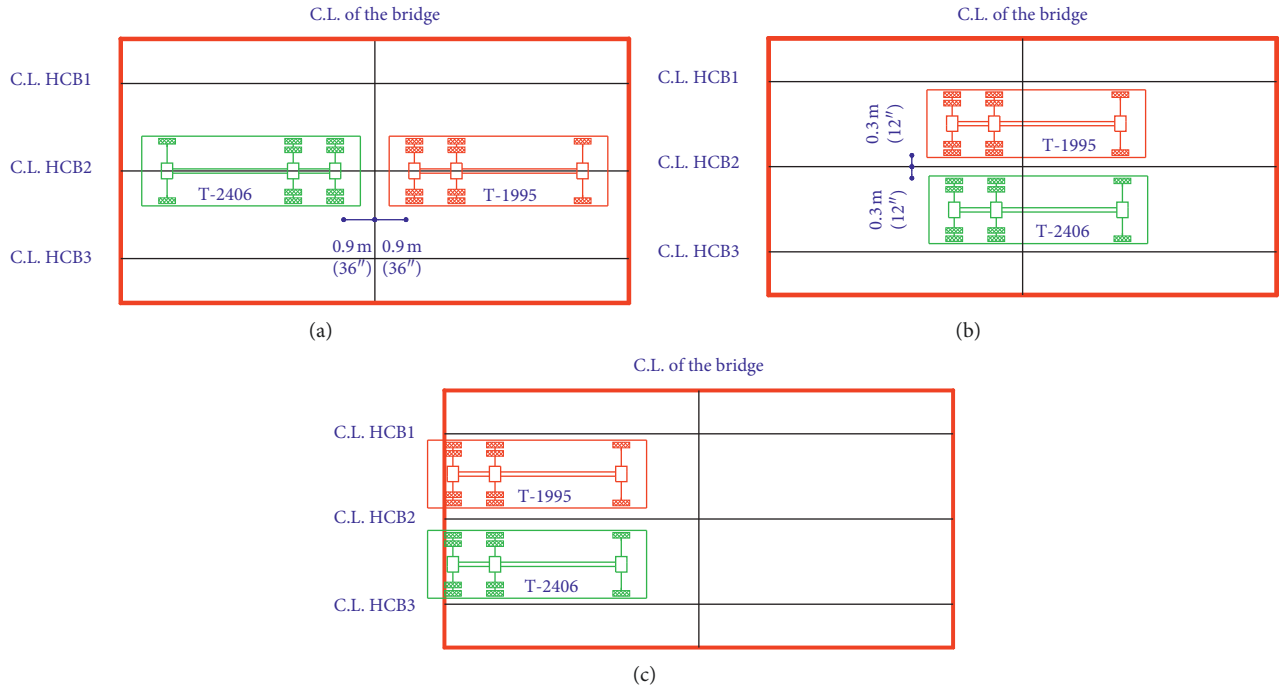

Figure 3: Load testing truck stops. (a) stop 1. (b) stop 2. (c) stop 3.

where f'_c is the compressive strength of concrete. In equations (1) and (2), f'_c, f_r, and E_c are in psi.

4.2. Steel Reinforcement. Two types of reinforcement bars were used in B0410. Typical Grade 60 mild steel reinforcing bars were used to reinforce the bridge deck, while seven-wire strands, conventional prestressed concrete strands (1860 MPa class) (Grade 270), were used in the HCBs. Young's modulus of the strand was assumed to be 196,500 MPa (28,500 ksi). The typical mild steel bars were assumed to have Young's modulus equal to 199,948 MPa (29,000 ksi). Both steel types were assumed to have Poisson's ratio of 0.3, and 7849 kg/m^3 (490 lb/ft^3) density.

4.3. FRP Composites. The laminate composition of the FRP shell of B0410 is a woven-glass reinforcing fabric with varying percentages of the fibers oriented in the 0°, 90°, and ±45° directions relative to the longitudinal axis. The matrix used to infuse the fibers is RTM-80545 vinylester resin. The shell was assumed to behave as orthotropic transversely isotropic material in the FEA. While in the mathematical calculations, only the longitudinal (0° direction) properties were used. The GFRP was assumed linear elastic up to failure. The manufacturer provided the mechanical properties of the shell. Poisson's ratio ν_{xy} was assumed to be 0.26, and ν_{yz} was assumed to be 0.30 [12]. A summary of the material properties used for modeling the FRP shell is listed in Table 1.

4.4. Polyisocyanurate Foam. Polyisocyanurate (polyiso) foam is a 32 kg/m^3 (2.0 lb/ft^3), rigid, closed cell foam supplied as blocks with 61 cm (24 in.) width. The elastic moduli and shear moduli were provided by the manufacturer in the longitudinal and perpendicular directions. In this study, the foam was assumed to behave as orthotropic transversely isotropic material. Since the compression and tension moduli are close to each other, the tension properties only were used in modeling the foam. Poisson's ratio ν_{xy} and ν_{xz} were assumed to be 0.33 [13]. A summary of the material properties used for modeling the polyiso foam is listed in Table 2.

5. Finite Element Modeling of Bridge 0410

The bridge superstructure was modeled via the commercial FEA software ANSYS 14. The FEM consisted of 224568 elements and 213634 nodes. The *Y*-axis was oriented in the gravity direction and the *X*-axis was oriented in the longitudinal direction of the beams, while the Z-axis was oriented in the lateral direction of the HCBs. Based on the mathematical predictions, all the materials were modeled as linear elastic. The results obtained from the FEMs also assured that all the materials behaved within their elastic range.

5.1. Element Types and Model Simplifications

5.1.1. Hybrid Composite Beam (HCB). The HCB was modeled using a combination of one-, two-, and three-dimensional space elements. The GFRP shell and the concrete web have small thicknesses relative to their lengths and widths; therefore, they were modeled using shell181 element. Shell181 is a four-node element with six degrees of freedom (DOFs) at each node. The concrete arch was modeled using solid65 element, and the polyiso foam was modeled using

Table 1: Material properties used for modeling the FRP shell.

Property	Strength MPa (ksi)	Stiffness GPa (msi)	Shear modulus GPa (ksi)
Tensile properties	$S_L^+ = 372\,(54)$	$E_x^+ = 27.6\,(4)$	$G_{xy} = 6.3\,(919)$
	$S_T^+ = 124\,(18)$	$E_y^+ = 15.7\,(2.3)$	$G_{xz} = 6.3\,(919)$
	$S_{LT} = 21\,(3)$	$E_z^+ = 15.7\,(2.3)$	$G_{yz} = 3.7\,(530)$
Compressive properties	$S_L^- = 138\,(20)$	$E_x^- = 8.96\,(1.3)$	$G_{xy} = 6.3\,(919)$
	$S_T^- = 152\,(22)$	$E_y^- = 9.5\,(1.4)$	$G_{xz} = 6.3\,(919)$
	$S_{LT} = 21\,(3)$	$E_z^- = 9.5\,(1.4)$	$G_{yz} = 3.7\,(530)$
Density kg/m^3 (lb/ft^3)		$\rho = 1682\,(105)$	

Table 2: Material properties used for modeling the polyisocyanurate foam.

Elastic modulus kPa (psi)	Poisson's ratio	Shear modulus kPa (psi)
$E_x^+ = 8440\,(1225)$	$\nu_{xy} = 0.33$	$G_{xy} = 1516\,(220)$
$E_y^+ = 3190\,(463)$	$\nu_{xz} = 0.33$	$G_{xz} = 1516\,(220)$
$E_z^+ = 3190\,(463)$	$\nu_{yz} = 0.308$	$G_{yz} = 1219\,(177)$

solid185 element. Both elements are eight-node elements having three translational DOFs at each node. The HCB strands were modeled using beam188 element, which has six DOFs at each node. The tension reinforcement is arranged in two layers that lie directly on the lower FRP flange. In the FEM, the strands were shifted upward and modeled in one layer separated from the lower flange by 2.54 cm (1 in.) of foam. To simplify modeling, the 44 strands were modeled via five separate beam elements. The total cross-sectional area of the five beam elements equals the cross-sectional area of the 44 strands. A perfect bond between all the components of the HCB was assumed. This was achieved by meshing all the constituents using the same mesh. Figure 4 displays the finite element modeling of HCB using ANSYS V14.

5.1.2. Bridge Deck. Solid65 elements were used to model the bridge concrete slab. Three solid elements were used throughout the slab thickness to allow modeling of the upper and lower reinforcement bars via beam188 elements. The parapet was poured simultaneously with the slab, and its reinforcement extended into the deck. Previous studies [3, 14] proved that when composite action is achieved between the slab and the parapet, the deflection and stress of the bridge girders are significantly decreased. Consequently, the parapet was included in the FEM and simulated using solid65 element. A Previous study [6] demonstrated that the shear connectors of the HCB achieved full composite action between the bridge deck and the HCBs. In the FEA, a perfect bond was assumed between the deck components and between the deck and the HCBs.

5.2. Modeling of Loads. In the first stage, the weight of the concrete arch and web was applied as uniform load on the lower foam elements (the foam elements below the concrete arch). In the second stage, the weight of the deck was applied as uniform load on the upper flange elements of the noncomposite HCB. In the last stage, the trucks axle loads were applied to the bridge superstructure as a uniform distributed load over each tire contact area on the upper surface of the deck elements. Finally, a linear superposition was performed between the three stages to obtain the total stresses in the different components of the HCB.

5.3. Modeling of Boundary Conditions. Each end of the HCBs of B0410 is supported on two steel-laminated neoprene bearing pads. Each elastomeric bearing pad, located underneath the chimney, is 30.5 cm × 30.5 cm × 1.9 cm (12–in. × 12–in. × 0.75–in.). The stress-strain behavior of an elastomer is controlled by the shear modulus and the shape factor of the elastomer [15]. According to AASHTO LRFD [16], the elastomer shall have a shear modulus from 0.655 MPa (95 psi) to 1.379 MPa (200 psi). In the current work, the shear modulus of the elastomer was assumed to be 1 MPa (145 psi). The shape factor, P, of rectangular elastomer layer is given by [16]

$$P = \frac{LW}{2h_{\mathrm{ri}}\,(L + W)}, \tag{3}$$

where L is the dimension of the bearing in the longitudinal direction of the beam (X-dir.), W is the dimension of the bearing normal to the longitudinal beam axis (Z-dir.), and h_{ri} is the thickness of a single elastomer layer.

A simplified equation based on the shear modulus, G, and the shape factor is provided by [17] to detect the stiffness of the bearings as follows:

$$E_{\mathrm{b}} = 6GP^2, \tag{4}$$

where E_{b} is the effective compressive modulus of the bearing.

Yazdani et al. [15] derived six translational and rotational stiffness values that can simulate the restrained forces and moments at the beam-pad interface. According to their study, the translational stiffness of the bearing in the X-dir.($k_{x\mathrm{b}}$) and the rotational stiffness about the Z-axis(k_{rzb}) are given by

$$k_{x\mathrm{b}} = \frac{CGA_{xz}}{H}, \tag{5}$$

$$k_{\mathrm{rzb}} = \frac{CE_{\mathrm{b}}I_z}{H}, \tag{6}$$

where A_{xz} is the area of the bearing in the xz plane, H is the total thickness of the bearing, I_z is the moment of inertia of the bearing about the Z-axis, and C is a factor that presents the effects of aging and cold temperatures on the elastomer

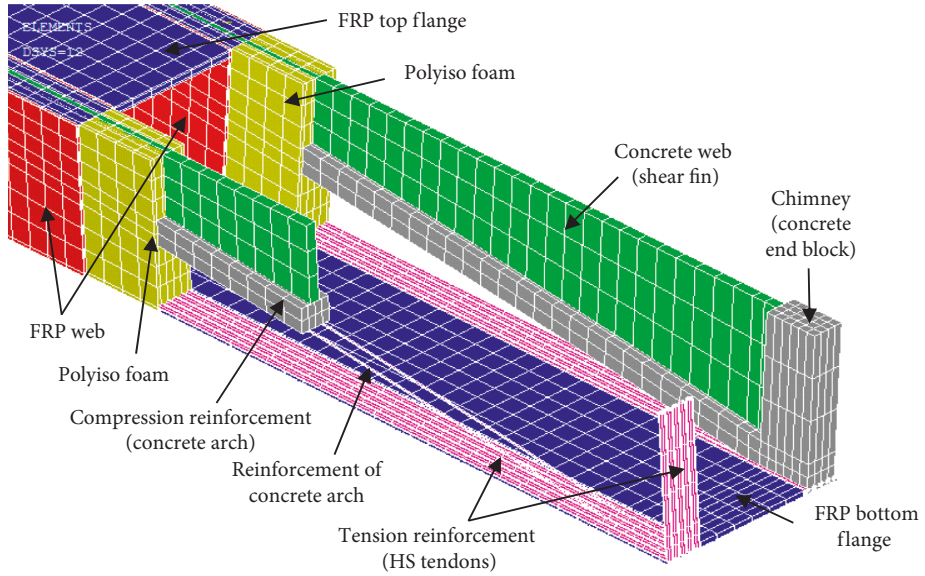

Figure 4: Finite element modeling of multicelled hybrid composite beam using ANSYS V14.0.

stiffness. The aging and temperature effects can increase the stiffness of the elastomer up to 50 times the original stiffness [18]. Based on the results obtained by [15], C was assumed to be 25 in the current study.

A previous FEA study of B0439, the first HCB bridge constructed in Missouri, revealed that modeling the bearing pads with pin supports that restrained the translational movements in all the directions led to acceptable predictions of the HCBs deflections [3]. In the current study, two models of B0410 superstructure were constructed with different boundary conditions to study the best simulation of the bearings effects. In the first model, the bearings were simulated via pin-pin supports similar to the previous study [3]. In the second model, the bearings were simulated by preventing the vertical movement in the gravity direction (Y-dir.), in addition to applying the translational and rotational springs given by equations (5) and (6), respectively. In the second model, the out-of-plane translational and rotational springs (k_{zb}, and k_{rxb} and k_{ryb}, respectively), derived by [15] were not applied because the bridge incorporates the use of concrete diaphragms that span between the HCBs ends and rest directly on the interior and exterior bents. These diaphragms were simulated in both models by applying supports that restrained the lateral translation of the HCBs at the contact areas between the diaphragms and the beams. The comparison between the field-measured strains produced by the three load stops and the FEM predictions showed that the second model achieved slightly better correlation with the experimental data. Consequently, the HCBs' supports in the second and third stages were simulated using roller supports combined with translational and rotational springs as done in the second model.

While the concrete arch was poured (the first stage); the HCB was supported on two concrete blocks. These blocks were assumed to prevent the displacement of the HCB in all directions. Consequently, in this stage, the HCB was modeled with pin supports at each end.

6. Mathematical Calculations

The current design methodology [5, 19], models the HCB as a straight, simply supported beam with varying sectional properties along the length of the beam. This procedure is based on the following assumptions:

(i) Plane sections that are perpendicular to the neutral axis (NA) before bending remain plane and perpendicular to the NA after bending (linear strain distribution throughout the HCB's depth)

(ii) The strain of different constituents at the same level is equal (a perfect bond between the beam's constituents)

(iii) The concrete below the NA has cracked and no longer contributes to the strength of the beam

The methodology uses the transformed area technique to transform the different constituents of the HCB to equivalent amounts of the GFRP of the webs. It calculates then the beam stiffness at $1/10^{\text{th}}$ points along the beam length to account for the nonprismatic nature of the beam's cross section. In the current work, the elastic neutral axis (ENA) and the stiffness at $1/20^{\text{th}}$ points along the beam length were determined, according to the current design procedure, as follows:

$$
\begin{aligned}
n_i &= \frac{E_i}{E_{\text{w}}}, \\
A_{tij} &= n_i A_{ij}, \\
\overline{y_j} &= \frac{\sum_{i=1}^{m} A_{tij} y_{ij}}{\sum_{i=1}^{n} A_{tij}}, \\
I_j &= \sum_{i=1}^{m} \left(I_{tij} + A_{tij} \left(y_{ij} - \overline{y}_j \right)^2 \right),
\end{aligned}
\tag{7}
$$

where n_i is the modular ratio of the component i, E_w is the modulus of elasticity of the FRP web, E_i is the elastic modulus of the component i, A_{ij} is the cross-sectional area of the component i at the section j, A_{tij} is the transformed area of the component i at the section j, y_{ij} is the distance from the c.g. of the component i to the extreme lower fiber of the beam at the point j, $\overline{y}_j$ is the distance from the ENA of the composite section to the extreme lower fiber of the beam at the section j, I_{tij} is the transformed moment of inertia of the component i with respect to its c.g. at the section j, I_j is the transformed moment of inertia of the composite section with respect to the ENA at the section j, m is the total number of the HCB components, and $j = 1, 2, \ldots, 21$.

The following AASHTO LRFD [16] equations were used to distribute the truck loads to HCB2:

$$g = \left(\frac{S}{3.0}\right)^{0.35}\left(\frac{Sd}{12.0L^2}\right)^{0.25} \text{(ASE)}, \tag{8}$$

$$g = \left(\frac{S}{6.3}\right)^{0.6}\left(\frac{Sd}{12.0L^2}\right)^{0.125} \text{(ASE)}, \tag{9}$$

where S is the spacing of the beams in feet, d is the depth of the beam in inch, and L is the span of beam in feet. Equation (8) was used when one lane was loaded, while equation (9) was used when two lanes were loaded.

Finally, the bending moments were calculated and the induced normal strains in the different components were obtained at each section via equation (10):

$$\varepsilon_{ij} = \frac{M_j\left(\overline{y}_j - y_{ij}\right)}{I_j E_w}, \tag{10}$$

where ε_{ij} is the normal strain of component i at the section j and M_j is the bending moment at section j.

7. Modified Methodology

Two modifications were applied to the current design methodology to enhance the strain estimation in the different components of the HCB. One modification was applied to the beam geometry while the other was applied to its boundary condition.

Due to the parabolic profile of the compression reinforcement, both horizontal movements and normal forces are expected to induce through the beam's length. Consequently, the stresses and strains are expected to be sensitive to the type of translational restraint that is provided at the end of the beam in its longitudinal direction (X-dir.). The current design methodology models the HCB as a straight simply supported beam. Therefore, neither axial forces induce through the beam nor the model is sensitive to the restrained translational DOFs in the longitudinal direction. It was noticed, during the mathematical modeling of the current bridge discussed herein, B0410, and B0439 [3], that the ENAs of the noncomposite and composite HCB (stages 2 and 3) form curved path. This path begins at the bottom at the supports with an apex at the center of the beam. Therefore, the first modification was achieved by modeling the HCB as a curved beam based on the ENAs' locations rather than modeling it as a straight beam.

The second proposed modification was performed by modeling the supports at each end with a roller support, preventing the displacement in the Y-dir., a translational spring in the X-dir., and a rotational spring about the Z-axis. Under static vertical loads, both the FRP shell and the strands are expected to deform downward only while the concrete arch is expected to perform horizontal and vertical movements. The horizontal deformation of the concrete arch is partially restrained by the strands at the beam's end, while the horizontal movement of the overall beam is partially restrained by the bearing pads at each end. Because the concrete arch is the source for the HCB's horizontal movement under static vertical loads, it may be acceptable to simulate the restrained horizontal forces at each end of the beam using a translational spring with the following stiffness:

$$K_x = K_{x\text{b}} + K_{xs}, \tag{11}$$

where K_x is the translational spring stiffness at the end of the HCB in the X-dir., $K_{x\text{b}}$ is the stiffness presented by the bearing pad and is given by equation (5), and K_{xs} is the stiffness provided by the strands.

It can be shown that K_{xs} is given by the following equation:

$$K_{xs} = \frac{2E_s A_s}{L}, \tag{12}$$

where E_s and A_s are the elastic modulus and the cross-sectional area of the strands, respectively.

The stiffness of the rotational springs at the HCB ends was calculated with equation (6). Then, the strains were estimated by modifying equation (10) to account for the axial force in the beam:

$$\varepsilon_{ij} = \frac{M_j\left(\overline{y}_j - y_{ij}\right)}{I_j E_w} + \frac{N_j}{A_j E_w}, \tag{13}$$

where N_j is the axial force at section j and A_j is the transformed cross-sectional area of the composite section at j.

The proposed modifications were applied only to the second and third stages. In the first stage (the HCB, without compression reinforcement), the ENA is at the same location along the beam length. Consequently, the beam was modeled as a straight beam without any modification to the existing methodology.

8. Results Discussion

Figures 5 and 6 display the measured and estimated normal strains in the different elements of the HCB2 that resulted from the three stops loads (stage 3) and casting the concrete arch (stage 1), respectively. Figure 7 illustrates only the estimated strains in the HCB2 that were produced by the second stage loads and the total loading of the three stages. The total loads from the three stages were obtained by adding stop 2 loads to the first and the second stage loads.

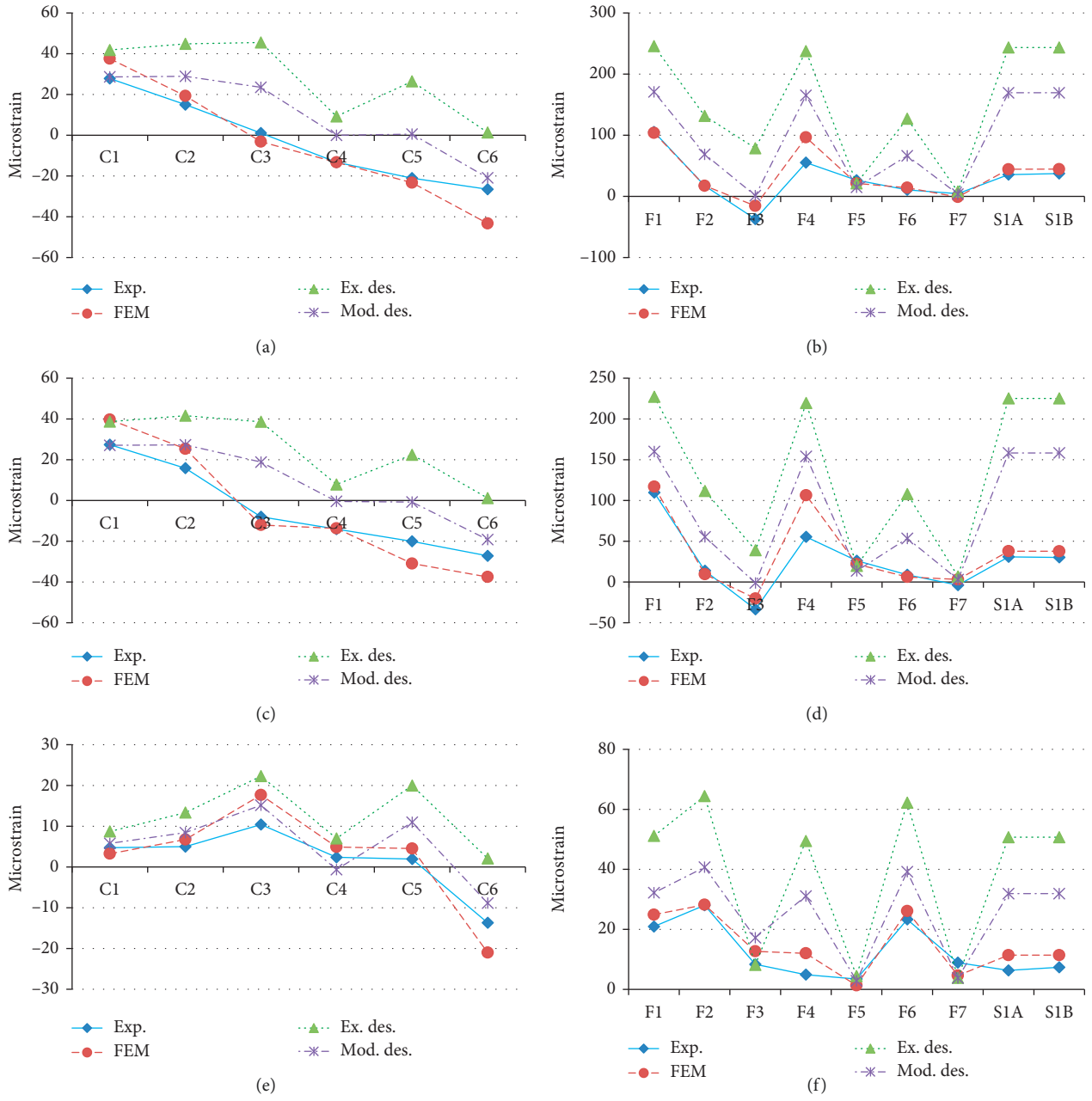

FIGURE 5: Strain values due to the three stops (stage 3). (a) Concrete VWSGs (stop 1). (b) FRP and steel gauges (stop 1). (c) Concrete VWSGs (stop 2). (d) FRP and steel gauges (stop 2). (e) Concrete VWSGs (stop 3). (f) FRP and steel gauges (stop 3).

The results clarify that the field-measured strains agree with the strains estimated by the FEM during the first and third stages.

The results clarify that the FEM predicted higher strains in the concrete arch than the measured strains under the three stops loads. Because the mix design of the concrete arches in B0410 contained fly ash, the arch may have gained strength higher than that was used in the FEM. Various studies [20, 21] have found that the fly-ash concrete achieves a significant increase in the strength after 28 days, and this increase in strength continues at the long-term due to the pozzolanic reaction. In general, the differences between the FEM predictions and the measured strains are within the expected range of errors for full-scale bridge testing. Consequently, the FEM was used here to analyze the flexural behavior of the HCB. It was also used as a reference to evaluate the performance of both the current and the modified methodologies in estimating the strains due to the second stage and total loading.

In the three stops, the maximum compressive stresses in the concrete arch were found to be very close to the junction of the arch with the chimney. Figures 5(a), 5(c), and 5(e) illustrate that the VWSG (C6), instrumented at this location, captured the maximum normal compressive strains due to

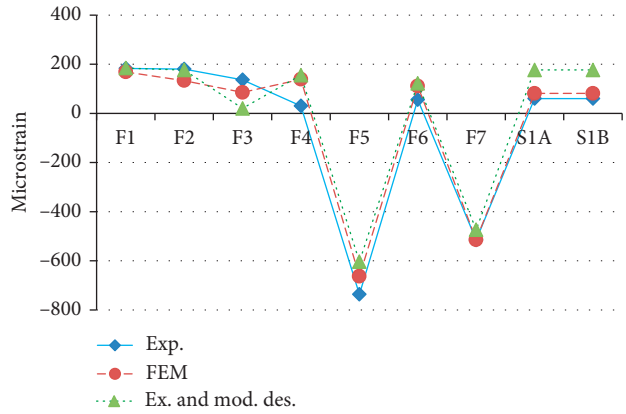

Figure 6: Strain values due to the concrete arch pour (stage 1).

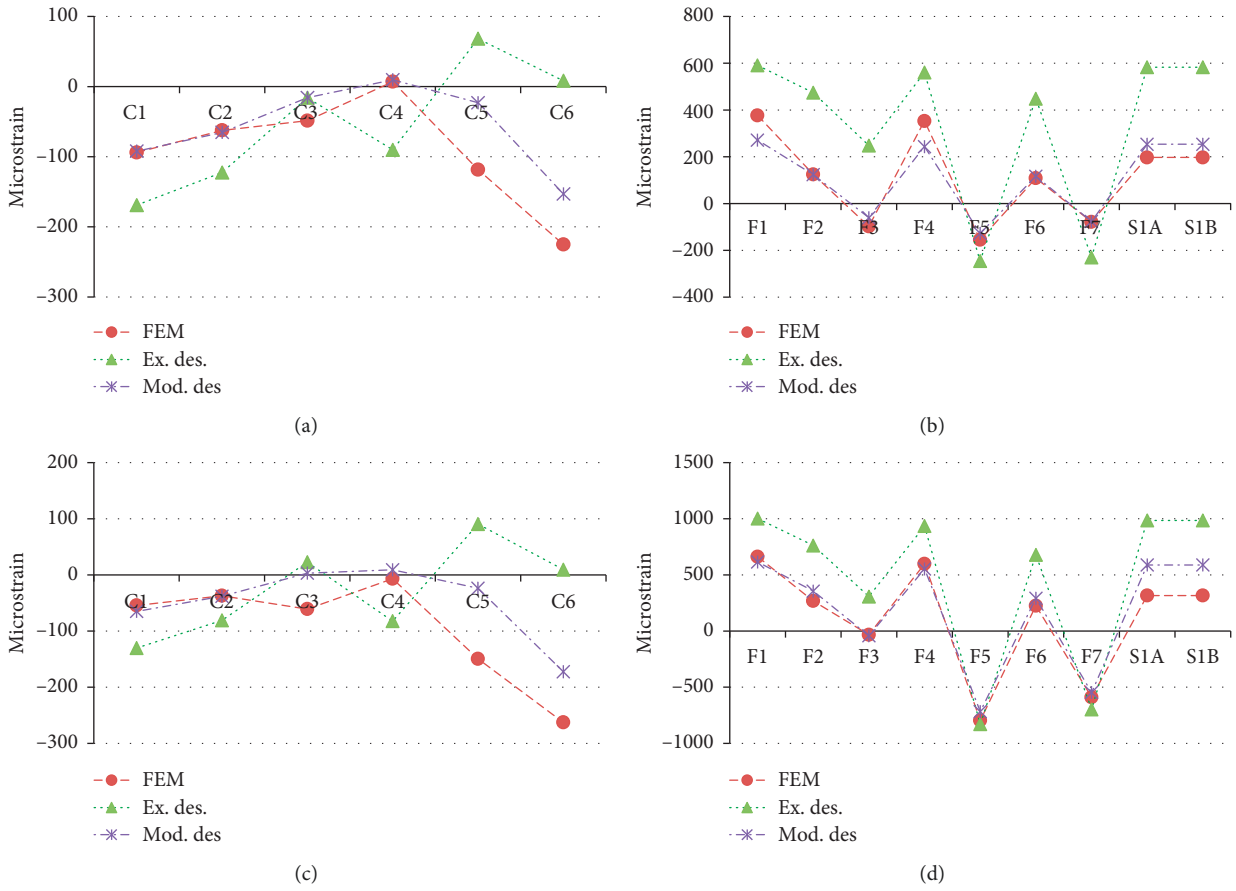

Figure 7: Strain values due to the deck pour (stage 2) and total loads of the three stages. (a) Concrete VWSGs (stage 2). (b) FRP and steel gauges (stage 2). (c) Concrete VWSGs (total load). (d) FRP and steel gauges (total load).

all the truck stops. Figure 8 illustrates that the same behavior was predicted by the FEM. According to the existing design model, C6 is located below the ENA in all of the stops and the bending moment is small at this location. Consequently, the current model always predicted very small tensile strains at C6. Figures 5(b) and 5(d) illustrate that the FRP strain gauge F3 captured compressive strains during stops 1 and 2. These results indicate that the HCB was subjected to negative bending moment at the support locations due to the restrained moments at the beam-pad interface. The negative moment may be combined with an axial compressive force along the beam length due to the parabolic profile of the compression reinforcement.

In general, the comparison between the field strains and the current design procedure strains shows that the methodology is accurate in predicting the strains in the first stage (where the HCB is prismatic along its length). The comparison also clarifies that the model is unable to predict

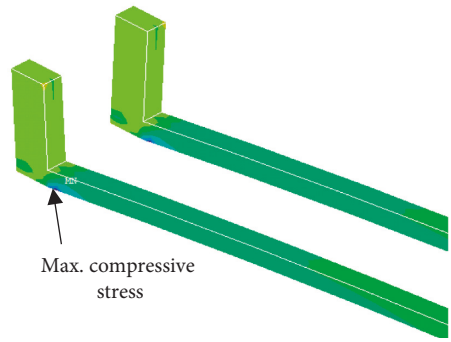

Figure 8: Normal stresses in concrete arches of HCB2 due to stop 1.

the maximum compressive stresses in the concrete arch and significantly conservative when predicting the tensile stresses in the FRP shell and strands in the third stage. The same trend was observed in the second stage, based on the FEM predictions. This behavior can be attributed to neglecting the negative moment at the beam end and the axial force through the beam. When the noncomposite HCB of B0410 was modeled with a pin support at one end and a roller support at the other end, the maximum compressive stress in the concrete arch was found at the same location and negative bending was observed at the end of the beam.

In a previous study, the writers attributed the negative moment at the beam end of the simply supported HCB to partial fixation provided by the chimney to the beam end [3]. The maximum compressive stress at this location may result from the negative moment combined with compressive axial force in the arch. Since the bearing stiffness has been documented to affect the bridge girders' behavior [15, 22], it is assumed here that the bearing stiffness is the primary cause of the negative moment at the HCB's end. Consequently, no definite conclusion regarding the chimney stiffness effect can be drawn from the experimental results collected in this study.

Figures 5(b), 5(d), and 5(f) illustrate that the measured strains at the strands midspan (S1A and S1B) are significantly lower than the bottom flange strains at the same location (F1). In the FEM, the strands were separated from the lower flange by 2.54 cm (1–in.) of foam; a perfect bond was assumed to exist between all of the superstructure's components. If the HCB has perfect beam behavior, the strains in the strands and the bottom flange should be very close to each other. However, similar differences as to what was measured experimentally, was detected by the FEM. These differences indicated that some of the design assumptions may be invalid. Thus, the FEM results were used to develop strain profiles throughout the thickness of the composite and noncomposite HCBs to verify the design assumptions.

The strain profiles at section (A-A), due to stop 1, and section (D-D), due to stop 3, are presented in Figure 9(a) and 10(a), respectively, while the strain profile of the noncomposite HCB at section (C-C) is displayed in Figure 10(b). Figures 9 and 10 also display the strain profiles obtained by the modified methodology (which is based on the same assumptions the current methodology is based on). In these figures, the FEM strains in the concrete arch and web, the strands, the FRP shell, and the concrete of the deck are denoted by CM, SM, FM, and DM, respectively. The strain profiles show that the assumption "the strain of different constituents at the same level is equal" is invalid. Reference [8] also noticed a strain incompatibility between the concrete arch and the GFRP shell, a finding that agrees with the FEM results presented in this study. The strain incompatibility between the HCB components can be attributed to the low shear moduli of the polyiso foam. This foam behaves as a flexible shear connection allowing differential vertical and horizontal displacements between the HCB elements.

Figure 9(b) illustrates the displacement in X-dir. of the composite HCB elements, at the midspan of the beam, due to stop 1. Vertical differential movements between the HCB components were also detected by the FEM. Mascaro and Moen [7] recorded relative vertical movements between the concrete arch and the FRP shell using two experimental methods: close-range photogrammetry and LVDT measurements. Their experimental investigations also agree with the current FEM results. Due to the relative movements between the HCB elements, the strain distribution throughout the deck, concrete arch, and concrete web is linear (because of the rigid connection between them) and the strain distribution through the GFRP shell components is linear but with different slope, while the strain in the strands is independent. The effect of the flexible shear connections on the strain throughout girders' depth has been documented by many researchers among them [23].

The FEM results demonstrated that the stress was not constant along the strands' length. Hillman [5] noticed the same behavior while testing the first HCB prototype. He concluded that the HCB behaves like a beam rather than a tied arch. In the current study, the strands, however, were found to be continuously subjected to tensile stresses, even where the FRP lower shell had compressive stresses. This indicates that the strands are subjected to an axial force at the HCB's end. Consequently, they work as a tie for the concrete arch while, at the same time, contributing to the beam's flexural rigidity. When Snape and Lindyberg [9] loaded a HCB up to failure, the failure occurred when the anchoring of the tension reinforcement broke free at end of the beam. This behavior supports the conclusion that the strands are subjected to an

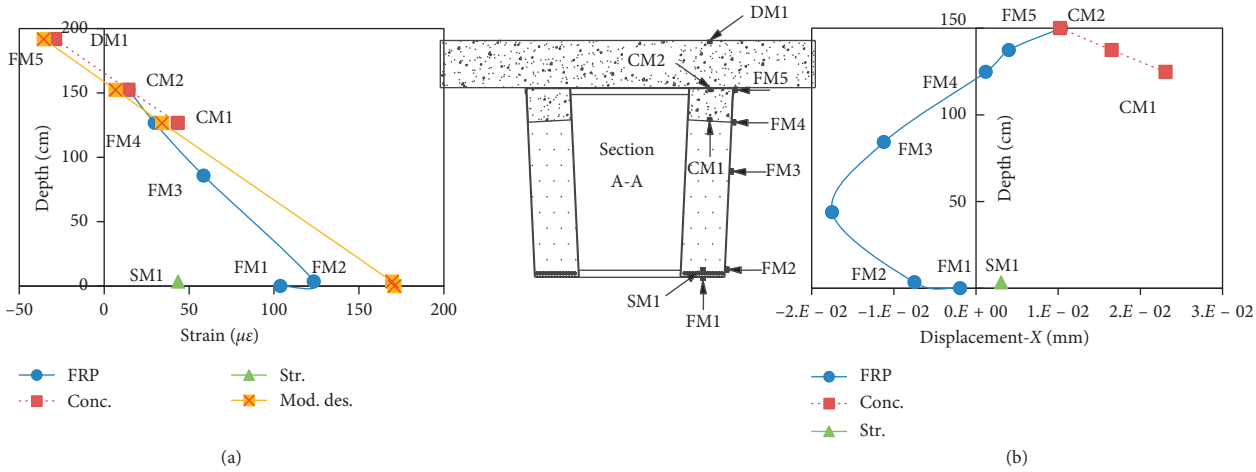

Figure 9: (a) Strain profile. (b) Displacement in X-dir. due to stop 1 section A-A.

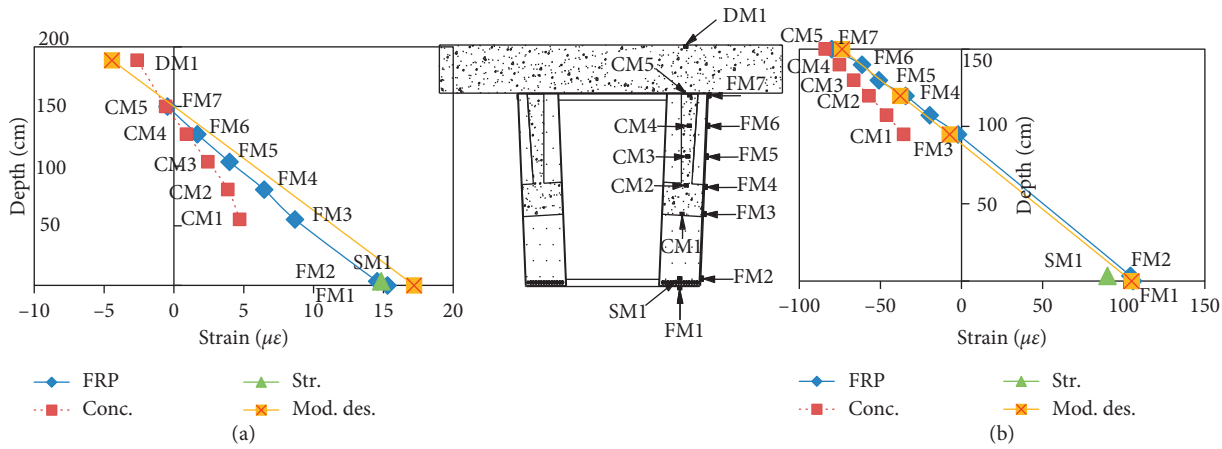

Figure 10: (a) Strain profile due to stop 3 section D-D. (b) Strain profiles due to stage 2 loads section C-C (noncomposite HCB).

axial force at the beam's end, restraining the horizontal movement of the arch as assumed by equation (11).

Figure 9(a) illustrates a difference between the strains at the bottom flange and the web (FM1 and FM2). Similar differences were noticed at other sections and can be attributed to the differential movement between the strands and the bottom flange. Because of this displacement, shear stresses are induced at both the strand-foam and flange-foam interfaces, producing axial forces along the length of the strands and the bottom flange. In practice, these axial forces are expected to transfer between the strands and the bottom flange through the layer of resin that separates the two elements.

Including all of the aforementioned factors in the mathematical model seem challenging and would complicate the design process for several reasons, among them, the differential displacement between the HCB elements does not follow specific pattern at some sections as it is clarified by Figure 9(b). Even if the differential displacement is assumed to follow linear pattern to simplify driving an equation that relates the slippage to the distance in X-dir., the fact that the geometric properties are functions of the distance in X-dir., leads to complex differential equation that has no explicit solution. Consequently, no closed form solution can be obtained to identify the relative displacements between the different elements of the HCB. Consequently, the modified methodology considers only the bearing effects and the HCB's curved shape to simplify the design process.

Figure 5 demonstrates that the modified methodology achieved some enhancement in estimating the normal strain in the different HCB elements. However, this figure also illustrates that the methodology is unconservative in identifying the maximum compressive stress in the concrete arch, and it cannot accurately identify the strains in some of the arch locations. The same trend was observed in the second stage, as illustrated in Figure 7(a), suggesting that the axial compressive force induced in the arch may be higher than that predicted by the modified methodology especially close to the beam end. Due to the partial composite action between the HCB constituents, the arch may have axial compressive force that is not proportioned to the axial forces of the other elements through their extensional stiffnesses as suggested by equation (13).

Figures 7(c), 7(d), 9, and 10 illustrate that although the strain incompatibility between the different HCB elements was ignored, the design methodology, proposed in the current study, achieved an acceptable accuracy when

identifying the normal strains in the HCB elements under the service loads. The results obtained by this methodology are comparable to the results estimated by very complex and time-consuming FEM. Moreover, the modified methodology is as simple as the current one and suits the daily design. However, it is clear that this methodology is applicable only to the service loads; its applicability to the ultimate strength design of the HCB needs to be verified experimentally.

The results of this study suggest that during the flexural design of the HCB, it is important to study the stresses at two sections, the midspan and the end of the beam, rather than the midspan only. They suggest also the need to include the bearing stiffness effects during the design of the HCB in bridge applications. Since the bearing stiffness is time-temperature dependent, it may be advisable to design two cases that include two extreme values for the temperature and aging parameter (C in equations (5) and (6)) that are expected to take place during the lifetime of the bridge (for example 1 and 50 based on [18]. The lower C value will create maximum stresses at the midspan while the larger value will create the maximum stresses at the beam's end.

9. Conclusions

A new HCB was recently used to construct three bridges in Missouri, USA. Due to the novelty of the HCB and its unclear behavior, this paper sought to examine its current flexural design methodology and assumptions, provide better understanding for the HCB's flexural behavior, and propose modifications to the current design model. The linear FEA was found accurate in predicting the normal stresses of the HCB under the service loads. The FEM clarified that the polyiso foam works as a flexible shear connection. In doing so, this foam achieves partial composite action between the different HCB elements producing differential displacement between them. Consequently, the different components at the same level have different strains. The current design methodology was found unable to predict the maximum compressive stress in the concrete arch because the procedure ignores both the restrained moments at the beam-pads interface and the curved shape of the beam. The findings of this study suggest that the HCB has no perfect beam behavior. The tied arch, including the chimneys, affects its flexural behavior. A modified procedure, based on the same assumptions as the existing one, was proposed. The proposed algorithm accounted for the effect of the tied arch by modeling the HCB as curved beam rather than straight one. Moreover, it simulated the effect of the tie on the beam behavior by applying translational springs at the beam-ends. The stiffness of these springs was derived based on the extensional stiffness of the tying reinforcement. The proposed methodology achieved significant enhancement in predicting the normal strains in the different HCB elements. The results obtained by this modified procedure suggest that it is acceptable, during the flexural design of the HCB, to ignore the relative movements between the HCB components assuming strain compatibility between them. This proposed methodology was examined using service loads only. Future work should investigate the applicability proposed within to the design of the ultimate flexural strength of the member.

Data Availability

The data used to support the findings of this study are available from the corresponding author upon request.

Conflicts of Interest

The authors declare that they have no conflicts of interest.

Acknowledgments

The authors would like to acknowledge the Missouri Department of Transportation (MoDOT) and the National University Transportation Center (NUTC) at Missouri S&T for sponsoring this research study. The staff support from the Dept. of Civil, Architectural & Environmental Engineering and Center for Infrastructure Engineering Studies (CIES) at Missouri S&T is also greatly appreciated.

References

[1] A. Mirmiran, "Innovative combinations of FRP and traditional materials," in *Proceedings of International Conference on FRP Composites in Civil Engineering*, vol. 2, Hong Kong, China, December 2001.

[2] R. C. Earley, M. A. Aboelseoud, and J. J. Myers, "Early-age behavior and construction sequencing of hybrid composite beam (HC beam) bridges in Missouri, USA," in *Proceedings of 11th International Symposium on Fiber Reinforced Polymer for Reinforced Concrete Structures*, Guimarães, Portugal, June 2013.

[3] M. A. Aboelseoud and J. J. Myers, "Finite element modeling of hybrid composite beam bridge in Missouri, USA," *Journal of Bridge Engineering*, vol. 20, no. 1, 2014.

[4] S. Ahsan, "Evaluation of hybrid-composite beam for use in tide mill bridge," M. S. thesis, Polytechnic Institute and State University, Blacksburg, VA, USA, 2012.

[5] J. R. Hillman, "Investigation of a hybrid-composite beam system," Final Report for High-Speed Rail IDEA Project 23, Transportation Research Board of National Academies, Chicago, IL, USA, 2003.

[6] J. R. Hillman, "Product application of a hybrid-composite beam system," HSR IDEA Program Final Report, Transportation Research Board of National Academies, Chicago, IL, USA, 2008.

[7] M. G. Mascaro and C. D. Moen, "Out-of-plane web deformation and relative arch movement of hybrid-composite beams based on photogrammetry," Report CE/VPI-ST-12/08, Virginia Polytechnic Institute and State University, Blacksburg, VA, USA, 2012.

[8] S. V. Nosdall, "Experiments on a hybrid composite beam for bridge applications," M. S. thesis, Virginia Polytechnic Institute and State University, Blacksburg, VA, USA, 2013.

[9] T. Snape and R. Lindyberg, "Test results: HC beam for the knickerbocker bridge," AEWC Report 10-16, University of Maine, Orono, ME, USA, 2009.

[10] P. L. Domone, "A review of the hardened mechanical properties of self-compacting concrete," *Cement and Concrete Composites*, vol. 29, no. 1, pp. 1–12, 2007.

[11] ACI, *Building Code Requirements for Structural Concrete (ACI 318-11) and Commentary*, American Concrete Institute, Farmington Hills, MI, USA, 2011.

[12] D. Kachlakev, T. Miller, S. Yim, K. Chansawat, and T. Potisuk, "Finite element modeling of reinforced concrete structures strengthened with FRP laminates," Final Report SPR 316, Oregon Department of Transportation Research Group & Federal Highway Administration, Washington, DC, USA, 2001.

[13] E. A. Friis, R. S. Lakes, and J. B. Park, "Negative Poisson's ratio polymeric and metallic foams," *Journal of Materials Science*, vol. 23, no. 12, pp. 4406–4414, 1988.

[14] J. J. Myers, D. J. Holdener, W. Merkle, and E. Hernandez, "Preservation of Missouri transportation infrastructures: validation of FRP composite technology through field testing, in-situ load testing of bridges P-962, T-530, X-495, X-596 and Y-298," Report no. OR09-007, Missouri Department of Transportation, Jefferson City, MO, USA, 2008.

[15] N. Yazdani, S. Eddy, and C. S. Cai, "Effect of bearing pads on precast prestressed concrete bridges," *Journal of Bridge Engineering*, vol. 5, no. 3, pp. 224–232, 2000.

[16] AASHTO LRFD, *AASHTO LRFD Bridge Design Specifications*, American Association of State Highway and Transportation Officials, Washington, DC, USA, 2012.

[17] AASHTO, *Standard Specifications for Highway Bridges*, American Association of State Highway and Transportation Officials, Washington, DC, USA, 1996.

[18] C. W. Roeder, J. F. Stanton, and T. Feller, "low temperature behavior and acceptance criteria for elastomeric bridge bearings," NCHRP Report 325, National Research Council, Washington, DC, USA, 1989.

[19] J. R. Hillman, *Hybrid-Composite Beam (HCB®) Design and Maintenance Manual*, Missouri Department of Transportation, Jefferson City, MO, USA, 2012.

[20] S.-H. Han, J.-K. Kim, and Y.-D. Park, "Prediction of compressive strength of fly ash concrete by new apparent activation energy function," *Cement and Concrete Research*, vol. 33, no. 7, pp. 965–971, 2003.

[21] K. Hwang, T. Noguchi, and F. Tomosawa, "Prediction model of compressive strength development of fly-ash concrete," *Cement and Concrete Research*, vol. 34, no. 12, pp. 2269–2276, 2004.

[22] C. S. Cai and M. Shahawy, "Predicted and measured performance of prestressed concrete bridges," *Journal of Bridge Engineering*, vol. 9, no. 1, pp. 4–13, 2003.

[23] T. Keller and H. Gürtler, "Design of hybrid bridge girders with adhesively bonded and compositely acting FRP deck," *Composite Structures*, vol. 74, no. 2, pp. 202–212, 2006.